Measurement of excitation functions of evaporation residues in the ^{16}O + ^{124}Sn reaction and investigation of the dependence of incomplete fusion dynamics on entrance channel parameters

D. Singh,[1,*] Sneha B. Linda,[1] Pankaj K. Giri,[1] Amritraj Mahato,[1] R. Tripathi,[2] Harish Kumar,[3] Suhail A. Tali,[3]
Siddharth Parashari,[3] Asif Ali,[3] Rakesh Dubey,[4] M. Afzal Ansari,[3] R. Kumar,[4] S. Muralithar,[4] and R. P. Singh[4]
[1]*Centre for Applied Physics, Central University of Jharkhand, Ranchi-835 205, India*
[2]*Radio-chemistry Division, Bhabha Atomic Research Centre, Mumbai-400 085, India*
[3]*Department of Physics, Aligarh Muslim University, Aligarh-202 002, India*
[4]*Inter-University Accelerator Centre, Aruna Asaf Ali Marg, New Delhi-110 067, India*

(Received 9 March 2018; revised manuscript received 3 May 2018; published 11 June 2018)

Excitation functions for the 11 evaporation residues populated through complete and/or incomplete fusion in ^{16}O + ^{124}Sn system at low projectile energies ≈3−7 MeV/nucleon have been measured. Recoil catcher activation technique followed by offline γ-ray spectrometry has been employed. Some of the evaporation residues are found to have contributions from precursor decays. The precursor contributions have been separated out from the measured cumulative cross-sections of evaporation residues. Independent cross-sections are compared with statistical model code PACE-4 predictions. The evaporation residues produced through xn and pxn channels are found to be well reproduced with the PACE-4 predictions after subtraction of precursor decay contributions. A substantial enhancement in the measured excitation functions over their theoretical predictions for the evaporation residues produced in α-emitting channels has been observed, which is attributed to the presence of incomplete fusion of projectile with target at these low energies. The present study shows that the incomplete fusion and the break-up probability of the incident ^{16}O into α clusters (i.e., break-up of ^{16}O into ^{12}C + α and/or ^{8}Be + ^{8}Be) increases with projectile energy. The present data suggests that the deformation of target is highlighting the important role to affect the ICF reactions independently with different projectiles. The comparison of the present study with literature data also shows that the ICF probability depends on various entrance channel parameters, namely, projectile energy, entrance channel mass-asymmetry, α-Q value, Coulomb factor ($Z_P Z_T$), deformation parameter (β_2), and their combinations. Moreover, the combined parameters $Z_P Z_T \cdot \beta_2$ and $\mu_{EC}^{AS} \cdot \beta_2$ are not found suitable to explain whole ICF characteristics, particularly for spherical and slightly deformed targets. On the other hand, the combined parameter $Z_P Z_T \cdot \mu_{EC}^{AS}$ has been found to explain more precisely the ICF dynamics as compared to other single and combined entrance channel parameters.

DOI: 10.1103/PhysRevC.97.064610

I. INTRODUCTION

The study of heavy ion-induced complete fusion (CF) and incomplete fusion (ICF) reactions at projectile energies above the Coulomb barrier has been a topic of resurgent interest. Several reaction channels are populated in the interaction of two heavy ions (heavier than α particle) when brought in contact with each other within the range of nuclear forces. The heavy ions (HIs)-induced reactions populate different evaporation residues with high excitation energy and angular momentum. Significant contribution in total fusion cross section from ICF has been observed at energies above the Coulomb barrier [1–9]. Semiclassically, the CF and ICF processes in HIs interaction can be categorized on the basis of different values of driving input angular momenta (ℓ) imparted in the system. According to the sharp cutoff approximation [10–12], the driving input angular momentum "ℓ" is distributed in the range $0 \leqslant \ell \leqslant \ell_{\rm crit}$ in the CF process in which the attractive nuclear potential overcomes the repulsive Coulomb and centrifugal potentials in central and near-central collisions. Consequently, in the collision of the projectile with the target with relatively lower value of impact parameter, CF dominates leading to the formation of a fully equilibrated compound nucleus (CN). However, in the collision of the projectile with the target with relatively higher values of energy and impact parameter, the repulsive centrifugal potential increases. Hence, the attractive nuclear potential ceases to capture the entire projectile. In such a situation, incomplete fusion occurs, in which only a part of the projectile fuses with the target nucleus and remnant projectile behaves as a spectator. For higher impact parameter collisions, the driving input angular momentum exceeds the critical limit ($\ell_{\rm crit}$), i.e., $\ell > \ell_{\rm crit}$ for CF and, therefore a part of the projectile is emitted to release excess driving input angular momentum. Thus, in ICF process, the driving input angular momentum ℓ is relatively larger compared to that for CF process. As such, prompt emission of a part of the projectile (predominantly α clusters) takes place, which reduces input angular momentum so that partial capture of the projectile may take place [13,14]. Ultimately, an incompletely fused composite system appears with relatively less charge and mass than the one populated by CF. The residual nuclei produced through the ICF process is

---

[*] dsinghcuj@gmail.com; dsinghiuac@gmail.com

therefore assumed to be associated with ℓ values above ℓ_{crit} for CF.

Morgenstern *et al.* [15] and Chakrabarty *et al.* [16] studied the entrance channel mass-asymmetry dependence of ICF by measuring the velocity spectra of heavy residues in different mass-asymmetric systems. In general, their study shows that for the same relative velocity, a more mass-asymmetric system has relatively higher ICF contribution than that of a less mass-asymmetric system. Studies have been done by Shuaib *et al.* [17] using measured excitation functions data to investigate the effect of Coulomb factor ($Z_P Z_T$) on ICF fraction. Further systematic studies have also been done by Kumar *et al.* [18], Yadav *et al.* [19], and Tali *et al.* [20] to investigate the effect of various entrance channel parameters (namely, entrance channel mass-asymmetry, α-Q value, $Z_P Z_T$) on ICF dynamics. These studies show that a single entrance channel parameter is not able to explain completely the incomplete fusion dynamics at low projectile energies.

Apart from experimental studies, several theoretical models have been proposed to understand the ICF dynamics. Break-up fusion (BUF) model of Tokugawa and Tamura [21] qualitatively explained the kinetic energy spectra and angular distributions of emitted particles. The sum-rule model of Wilczynski *et al.* [22] predicts that ICF mainly occurs in the peripheral interactions and are localized in angular momentum space above the critical angular momentum for the complete fusion (CF). However, Mermaz *et al.* [23] explained the energy and angular distribution of the projectile like fragments (PLFs) using a modified distorted-wave Born approximation (DWBA) formalism for surface transfer reactions. Other theoretical models are promptly emitted particles (PEP) model [24], hot spot model [25], and Fermi-jet model [26] were also proposed to explain various ICF observables. Though, several models are available to explain the measured ICF data at projectile energies $\geqslant$10 MeV/nucleon. None of those models are able to successfully explain the various features of measured ICF data at relatively low bombarding energies, i.e., 3–7 MeV/nucleon. A few systematic studies on excitation function of various projectile target systems have been done to investigate the dependence of ICF on various entrance channels parameters namely, projectile energy, projectile structure effect, entrance channel mass-asymmetry, Coulomb factor ($Z_P Z_T$), α-Q value. But none of these studies has been done to investigate the role of target deformation on ICF dynamics along with the combined parameters $\mu_{\text{EC}}^{\text{AS}} \cdot \beta_2$ and $Z_P Z_T \cdot \mu_{\text{EC}}^{\text{AS}}$ using EFs measurement of the evaporation residues.

The present work has been carried out to investigate the dependence of ICF dynamics on various entrance channel parameters at projectile energies above the Coulomb barrier. In the present study, excitation functions (EFs) for ERs produced through CF and ICF reactions in the $^{16}\text{O} + {}^{124}\text{Sn}$ system at the low projectile energies $\approx$3–7 MeV/nucleon has been measured. The measured EFs for several evaporation residues populated through CF and ICF reactions are compared with the predictions of statistical model code PACE-4 [27]. Present data along with those from literature have been analyzed to get information regarding dependence of incomplete fusion dynamics on various entrance channel parameters, namely, entrance channel mass-asymmetry ($\mu_{\text{EC}}^{\text{AS}}$), Coulomb factor ($Z_P Z_T$), deformation parameter (β_2), and their combinations $Z_P Z_T \cdot \beta_2$, $\mu_{\text{EC}}^{\text{AS}} \cdot \beta_2$, $Z_P Z_T \cdot \mu_{\text{EC}}^{\text{AS}}$.

The present paper is organized as follows. The experimental details are discussed in Sec. II. The procedure used for extraction of independent cross-sections from the measured cumulative cross-sections is given in Sec. III. The details of analysis of measured excitation functions in the framework of statistical model code PACE-4 is given in Sec. IV. The interpretations of experimental results are discussed in Sec. V. The systematic studies for dependence of ICF dynamics on various entrance channel parameters is described in Sec. VI. Finally, summary and conclusions of the present study are given in Sec. VII.

II. EXPERIMENTAL DETAILS

Present experiment for the measurement of EFs of different evaporation residues produced in $^{16}\text{O} + {}^{124}\text{Sn}$ system has been carried out at 15UD Pelletron heavy ion accelerator facility of the Inter University Accelerator Centre (IUAC), New Delhi, India.

A. Preparation and irradiation of targets

Enriched targets of ^{124}Sn with purity better than (97.4%) were prepared by vacuum evaporation technique at Target Laboratory of IUAC, New Delhi, India. The aluminium backing/degrader foils of thicknesses 1.2–1.7 mg/cm^2 were prepared by rolling technique for the deposition of ^{124}Sn material. The thickness of each aluminum and deposited ^{124}Sn material was determined by using microbalance as well as by the α particle transmission method using standard ^{241}Am source. The α particle transmission method is based on the measurement of the energy loss by 5.487 MeV α particles emitted from standard ^{241}Am-source, while passing through the target material. Enriched ^{124}Sn target material of desired thickness ($\approx$200–300 μg/cm^2) was deposited on Al-backings of thicknesses $\approx$1.2–1.7 mg/cm^2 foil of dimension 1.5 × 1.5 cm^2, which were pasted on the Stainless steel (SS) holders having concentric holes of diameter 1 cm. The Al backing along with deposited ^{124}Sn target material was pasted on SS target holders with silver collider paste for rapid heat dissipation during experiment.

In the experiment of excitation function measurement, targets were arranged in the form of the stack for irradiation. The irradiations have been carried out in the General Purpose Scattering Chamber (GPSC) at IUAC. The GPSC have in-vacuum transfer facility (IVTF). The GPSC along with IVTF has been used to minimize the lapse time between the stop of irradiation and starting of the counting. The targets in the stack along with catcher foils were arranged in such a way that target material faced the beam, so that the recoiled evaporation residues were trapped in the Aluminium backing and catcher foils. Two stacks of ^{124}Sn targets backed by thick aluminum catchers were irradiated at the beam energies $\approx$80 and $\approx$100 MeV, respectively. Each stack consisting of four targets was irradiated with $^{16}\text{O}^{7+}$ beam. Keeping in view the half-lives of interest, each stack of ^{124}Sn targets was

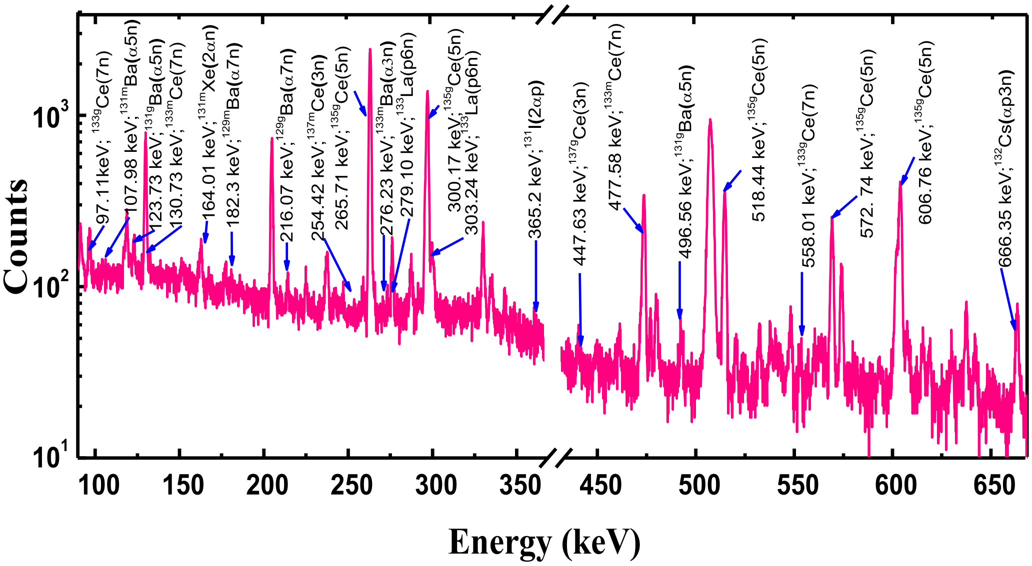

FIG. 1. Typical γ-ray spectrum showing γ lines of different evaporation residues populated via CF and/or ICF reaction in $^{16}O + ^{124}Sn$ system at beam energy 99.7 MeV.

irradiated for about ~7.5 h. The beam current was continuously monitored and was about 2 to 2.5 pnA in both irradiations. The beam flux was calculated by the total charge collected in the Faraday cup, which was placed using a current integrator device behind the target-catcher foil assembly. The energies of ^{16}O-ion beam on the successive targets have been calculated using stopping power software SRIM-2008 [28] based on energy-range formulations. In these calculations energy straggling effect has not been taken into account due to its insignificant contribution.

B. Energy and efficiency calibration of HPGe detector

A large number of evaporation residues are produced during the heavy-ion reactions at energy above the Coulomb barrier. The evaporation residues produced in heavy ion reactions have a large number of γ rays. In the present measurements, a high-resolution high-purity germanium (HPGe) detector of 100 cm^3 volume was used for the recording and subsequent identification of characteristic γ rays of ERs produced in $^{16}O + ^{124}Sn$ reaction. The detector was coupled to a PC through a CAMAC based CANDLE [29] software. The characteristic γ-ray energies, their abundances and half-lives of evaporation residue are taken from Refs. [30,31]. The standard γ-ray source and the irradiated samples were counted in the same geometry. The distance between the irradiated target and HPGe detector was adjusted so that the dead time of the HPGe detector was always less than 10%. After irradiation, the stacks of targets along with catcher foils were taken out quickly from the GPSC chamber. The evaporation residues produced were identified by their characteristic γ ray, branching ratio of γ-ray, and following their half-lives. The software CANDLE [29] has also been used for data analysis. The energy and geometry dependent photopeak detection efficiency calibration of the HPGe detector was carried out using standard ^{152}Eu γ-ray source of known strength.

C. Identification of evaporation residues

The decay of evaporation residues populated via CF and ICF processes leads to the emission of characteristic γ rays. For the determination of cross section of produced evaporation residues, it is necessary to identify their characteristic γ rays. After the irradiation, γ activity induced in the individual irradiated target-catcher (assembly) was recorded using a precalibrated high resolution HPGe detector coupled to a PC through CAMAC based CANDLE software. The γ-ray spectrum of each irradiated target-catcher was recorded at different times for decay curve analysis. The preliminary identification of evaporation residues have been done by their observed characteristic γ lines in γ-ray spectrum. Further, all evaporation residues were confirmed by their decay curve analysis. A typical γ-ray energy spectrum obtained from irradiated ^{124}Sn sample at beam energy of 99.7 MeV is shown in Fig. 1. Different γ-ray peaks have been assigned to evaporation residues produced through CF and/or ICF reaction channels. A list of identified ERs produced via CF and /or ICF reaction in $^{16}O + ^{124}Sn$ system and their decay data is given in Table I. The measured production cross-section σ for a particular reaction product has been computed using the expression given in Ref. [32].

A C^{++} program EXPSIGMA based on the above formulation has been used for the determination of formation cross-sections of the evaporation residues populated through CF and ICF reaction channels.

D. Errors and uncertainties in measurements

There are several factors which contribute to the uncertainties in the measured cross-sections of CF and/or ICF reaction. The main factors are discussed here: (i) fluctuations in the beam current during the irradiation of target may result in the variation of the measured cross-section. To keep the constant current during the target irradiation proper care has been taken.

TABLE I. List of identified evaporation residues populated via CF and/or ICF channels along with their half-lives, spin, γ-ray energies, and branching ratios.

Sr. No	Evaporation residues with channels	Half–life	Spin	$E\gamma$ (keV)	Branching ratio θ_1 (%)
1	$^{137\mathrm{m,g}}$Ce($3n$)	34.40 h (m)	$11/2^-$	254.42	11.0
		9.00 h (g)	$3/2^+$	447.63	1.8
2	^{135}Ce($5n$)	17.70 h	$1/2^+$	265.71	41.8
				300.17	23.5
				606.76	18.6
				518.44	13.6
				572.74	10.4
3	$^{133\mathrm{m,g}}$Ce($7n$)	4.93 h (m)	$9/2^-$	477.58	39.0
				130.73	17.9
		97.00 min (g)	$1/2^+$	97.11	45.0
				558.01	11.3
4	^{133}La($p6n$)	3.91 h	$5/2^+$	279.10	1.6
				303.24	1.1
5	$^{133\mathrm{m}}$Ba($\alpha 3n$)	38.90 h (m)	$11/2^-$	276.23	17.8
6	$^{131\mathrm{m,g}}$Ba($\alpha 5n$)	14.50 min (m)	$9/2^-$	107.98	55.0
		11.50 d (g)	$1/2^+$	496.56	47.0
				123.73	28.9
7	$^{129\mathrm{m,g}}$Ba($\alpha 7n$)	2.16 h (m)	$7/2^+$	182.30	15.7
		2.23 h (g)	$1/2^+$	216.07	13.4
8	$^{135\mathrm{m}}$Cs(αp)	53.00 min (m)	$19/2^-$	785.77	100.0
				847.33	95.9
9	^{132}Cs($\alpha p3n$)	6.48 d	2^+	666.35	98.0
10	$^{131\mathrm{m}}$Xe($2\alpha n$)	11.84 d (m)	$11/2^-$	164.01	1.9
11	^{131}I($2\alpha p$)	8.02 d	$7/2^+$	365.20	81.7

(m) = metastable state; (g) = ground state; min = minutes; h = hours; d = days

The error due to the fluctuations in beam current is estimated to be <6%. (ii) The uncertainty due to the nonuniformity of the target and uncertainty of the thickness measurement was estimated to be <3%. (iii) The uncertainty arising from the error in the efficiency calibration of the detector was estimated to be <5%. (iv) To minimize dead time losses, it was limited below 10%. (v) Uncertainty due to the straggling of the ion beam passing through the stack is estimated to be <2%. The overall uncertainty from all these factors including statistical errors in the photopeak area is estimated to be <15%.

III. EXTRACTION OF INDEPENDENT CROSS-SECTIONS FROM THE MEASURED CUMULATIVE CROSS-SECTIONS

Some of the radioactive evaporation residues are produced independently in the interaction of ^{16}O with ^{124}Sn and give rise to independent yield, while some of them are also produced by the decay of their higher and lower Z precursor isobars through $\beta^{\pm}$-emission and/or by EC process and give rise cumulative yield. If the half-life of the precursor is considerably smaller than that of the evaporation residue under investigation, for such cases, cumulative cross-sections of evaporation residues have been measured. The cumulative cross section for a given evaporation residue is the sum of (i) the cross-section for its independent production and (ii) the cross-section of cumulative/independent production of its precursors multiplied by numerical coefficient (F_{M_P}). This numerical coefficient may be greater than unity and depends upon the branching ratios for the decay of the precursors to the evaporation residue and on the half-lives of the precursor and the evaporation residue. An attempt has been made to separate out the contribution from precursor decay by using the prescription of Cavinato *et al.* [33]. Some of the expressions used for deducing independent cross-sections for those evaporation residues that have precursor contributions in ^{16}O + ^{124}Sn system are given in Table II.

The independent and cumulative cross-sections for all the measured residues are displayed in Figs. 2–5. Here, it is important to mention that for the evaporation residues $^{137\mathrm{m,g}}$Ce($3n$), ^{135}Ce($5n$), $^{133\mathrm{m,g}}$Ce($7n$), $^{133\mathrm{m}}$Ba($\alpha 3n$), $^{131\mathrm{m,g}}$Ba($\alpha 5n$), $^{129\mathrm{m,g}}$Ba($\alpha 7n$), $^{135\mathrm{m}}$Cs(αp), ^{132}Cs($\alpha p3n$), and $^{131\mathrm{m}}$Xe($2\alpha n$) no higher Z precursor contributions have been found in their decays, hence measured cross-section values are independent formation cross-sections of these evaporation residues. In case of evaporation residue $^{131\mathrm{m}}$Xe($2\alpha n$), it is not possible to separate out the independent contribution from their cumulative cross-section. In the analysis measured cumulative cross-sections has been compared with theoretical calculations based on PACE-4 for this ER.

IV. ANALYSIS OF MEASURED EXCITATION FUNCTIONS IN THE FRAMEWORK OF STATISTICAL MODEL CODE PACE-4.

The decay of the excited nuclei produced in HI reactions can be described by statistical model calculations. To examine

TABLE II. Deduced expressions used for the extraction of independent cross-sections from the measured cumulative cross-sections for ^{16}O + ^{124}Sn system.

Residues	Measurements	Expressions for the extraction of independent cross-sections
^{133}La	Independent	$\sigma^{\mathrm{meas}}_{\mathrm{cumt}}(^{133}\mathrm{La}) = \sigma^{\mathrm{meas}}_{\mathrm{indp}}(^{133}\mathrm{La}) + 1.71\sigma^{\mathrm{meas}}_{\mathrm{indp}}(^{133g}\mathrm{Ce})$
^{133m}Ba	Independent	$\sigma^{\mathrm{meas}}_{\mathrm{cumt}}(^{133m}\mathrm{Ba}) = \sigma^{\mathrm{meas}}_{\mathrm{indp}}(^{133m}\mathrm{Ba}) + 1.11\sigma^{\mathrm{meas}}_{\mathrm{indp}}(^{133}\mathrm{La}) + 1.20\sigma^{\mathrm{meas}}_{\mathrm{indp}}(^{133g}\mathrm{Ce})$

m = metastable state, g = ground state, indp = independent cross-section, cumt = cumulative cross-section, meas = measured

the decay of excited compound nucleus ^{140}Ce formed in ^{16}O + ^{124}Sn system, the measured excitation functions of evaporation residues are compared with statistical model code PACE-4 [27]. The code PACE-4 is based on the Monte Carlo simulation procedure used for the de-excitation of compound nucleus. The angular momentum projections are calculated at each stage of de-excitation. These angular momentum projections enable to determine the angular distribution of emitted particles. The CF cross-sections of the system are calculated using Bass formula [34]. Using optical model potentials [35], the transmission coefficient for light particles n, p, and α emission are determined. The γ-ray strength functions, required for transitions E1, E2, and M1 may either be taken from default or the tables of Endt [36]. The masses are read from the atomic mass table [37] in this code. A fission decay mode is employed using a rotating liquid drop fission barrier routine [38]. The ICF is not taken into account in PACE-4 calculations. Hence, the enhancement in the measured excitation functions (EFs) over PACE-4 predictions, for the evaporation residues that are produced in the break-up of projectile into α–clusters, may be attributed to the ICF process. The rotational energy of the decaying nuclei was calculated using the rotating liquid drop model. The level density parameter "a" ($=A/K$) MeV^{-1} is one of the important parameters in this code. Where "A" is the mass number of the compound nucleus and "K" is called level density parameter constant, which affects energy spectra

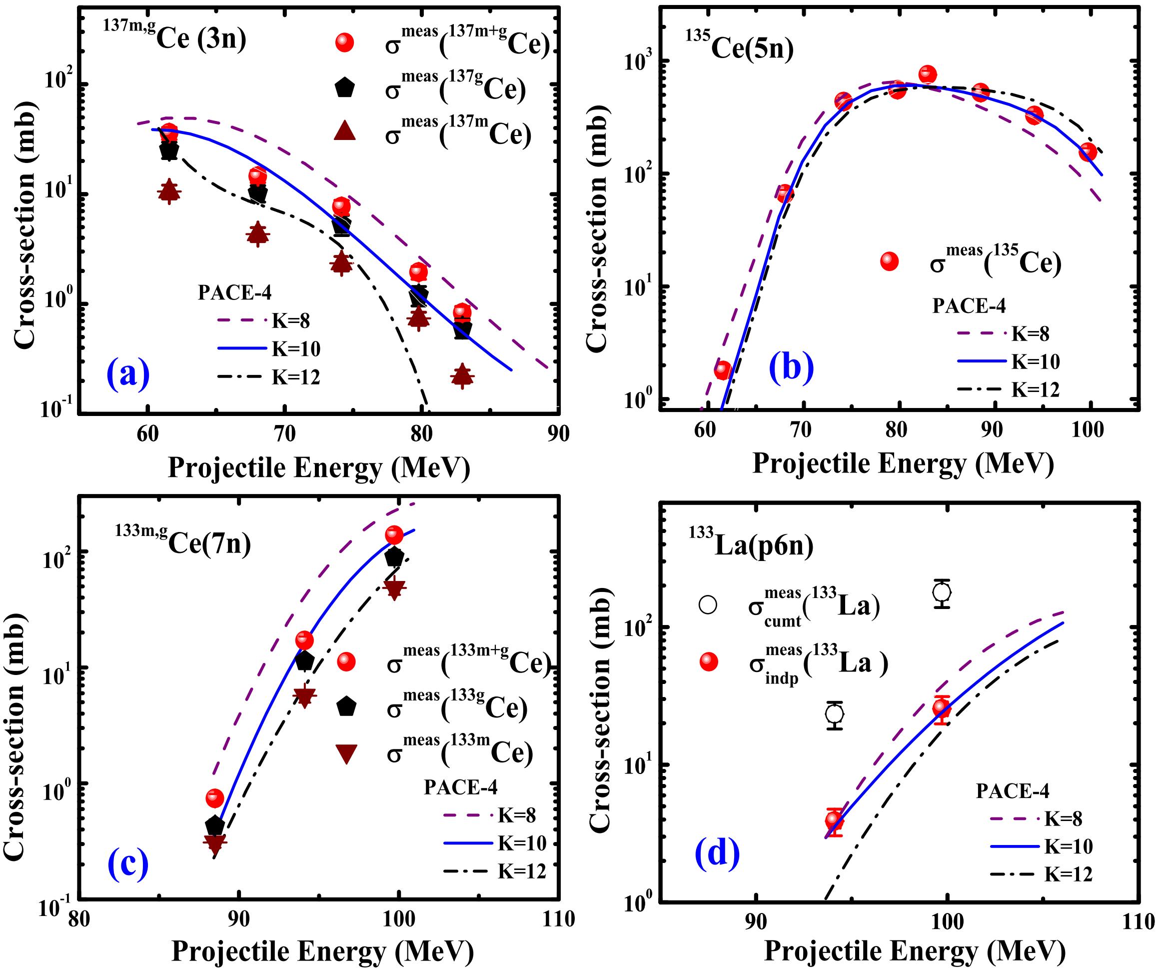

FIG. 2. Excitation functions for the ERs ^{137m,g}Ce($3n$), ^{135}Ce($5n$), ^{133m,g}Ce($7n$), and ^{133}La($p6n$) produced in ^{16}O + ^{124}Sn system. Solid and hollow symbols represent measured data. The dash, solid, and dash-dotted lines correspond to the theoretical predictions of PACE-4 code for K = 8, 10, 12, respectively.

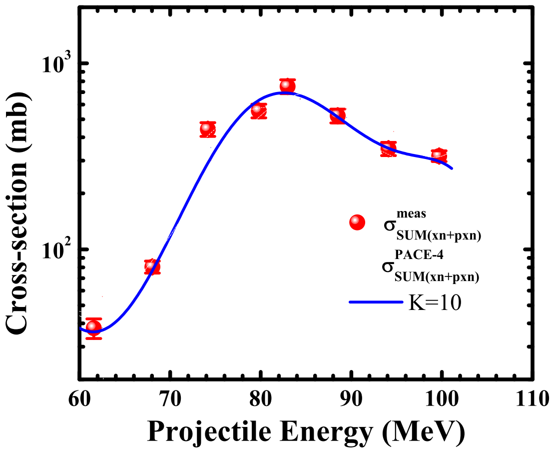

FIG. 3. Sum of all measured EFs of *xn* and *pxn* emission channels ($\sigma^{\mathrm{meas}}_{\mathrm{SUM}(xn+pxn)}$) populated in $^{16}\mathrm{O} + {}^{124}\mathrm{Sn}$ system along with PACE-4 predictions ($\sigma^{\mathrm{PACE-4}}_{\mathrm{SUM}(xn+pxn)}$) at $K = 10$.

of the emitted particles. Most of the required input parameters have been used as default except the mass and charge of the projectile and target nucleus.

V. INTERPRETATION OF EXPERIMENTAL RESULTS

The excitation functions for 11 evaporation residues $^{137\mathrm{m,g}}\mathrm{Ce}(3n)$, $^{135}\mathrm{Ce}(5n)$, $^{133\mathrm{m,g}}\mathrm{Ce}(7n)$, $^{133}\mathrm{La}(p6n)$, $^{133\mathrm{m}}\mathrm{Ba}(\alpha 3n)$, $^{131\mathrm{m,g}}\mathrm{Ba}(\alpha 5n)$, $^{129\mathrm{m,g}}\mathrm{Ba}(\alpha 7n)$, $^{135\mathrm{m}}\mathrm{Cs}(\alpha p)$, $^{132}\mathrm{Cs}(\alpha p3n)$, $^{131\mathrm{m}}\mathrm{Xe}(2\alpha n)$, and $^{131}\mathrm{I}(2\alpha p)$ produced in $^{16}\mathrm{O} + {}^{124}\mathrm{Sn}$ system have been measured. These measured excitation functions have been analyzed by employing the statistical model code PACE-4. In general, it is a well-known fact that almost all evaporation residues predominantly populated via CF reaction in the *xn*- and *pxn*-emitting channels can be reproduced by theoretical predictions of code PACE-4. The same input parameter is used to compare the measured EFs of all α-emitting channels. The enhancement in the measured EFs over their theoretical predictions for the α-emitting channels may be attributed to the ICF process, as PACE-4 code does not take ICF contribution into account.

A. *xn* and *pxn* emission channels (CF channels)

To study the reaction mechanism of evaporation residues populated via xn/pxn channels, an attempt has been made to reproduce the measured EFs of these evaporation residues using the statistical model code PACE-4. The level density "a" $((=A/K)\,\mathrm{MeV}^{-1}$ was varied by using different values of parameter K. The value of $K > 10$ may give rise to the anomalous effect in the particle multiplicity and CN temperature [39]. In the present work, $K > 10$ values have been used to observe the sensitivity of the theoretical excitation functions to this parameter. The effect of variation of "K" (= 8, 10, and 12) on the theoretical EFs along with the measured EFs for the ERs produced in the four reaction channels $^{137\mathrm{m,g}}\mathrm{Ce}(3n)$, $^{135}\mathrm{Ce}(5n)$, $^{133\mathrm{m,g}}\mathrm{Ce}(7n)$, and $^{133}\mathrm{La}(p6n)$ have been tested and are shown in Figs. 2(a)–2(d), respectively. No precursor contribution for the ERs $^{137\mathrm{m,g}}\mathrm{Ce}(3n)$, $^{135}\mathrm{Ce}(5n)$, and $^{133\mathrm{m,g}}\mathrm{Ce}(7n)$ have been observed. It is important to mention that the formation cross-sections for the $^{137\mathrm{m,g}}\mathrm{Ce}$ and $^{133\mathrm{m,g}}\mathrm{Ce}$ evaporation residues of ground as well as metastable states have been measured. The measured cross-sections of the ERs $^{137}\mathrm{Ce}$ and $^{133}\mathrm{Ce}$ of metastable as well as ground state along with the sum of ground- and metastable state contributions are displayed by respective symbols. The evaporation residue $^{135}\mathrm{Ce}$ (5n) is populated by emission of five neutrons from compound nucleus $^{140}\mathrm{Ce}^*$. The metastable state of a half-life of $\approx$20 s decays to the ground state by isomeric transition, which has a half-life of $\approx$17.7 h. The counting of the irradiated samples was done after complete decay of metastable state to their ground state of ER $^{135}\mathrm{Ce}$. The measured cross-section is the total cross-section of metastable and ground state. The measured EFs for the evaporation residues $^{137\mathrm{m,g}}\mathrm{Ce}$, $^{135}\mathrm{Ce}$, and $^{133\mathrm{m,g}}\mathrm{Ce}$ populated through xn ($x = 3$, 5 and 7) channels are shown in Figs. 2(a)–2(c), respectively. In these figures, the measured EFs for the ERs $^{137\mathrm{m,g}}\mathrm{Ce}$, $^{135}\mathrm{Ce}$, and $^{133\mathrm{m,g}}\mathrm{Ce}$ are found to be in good agreement with that theoretical predictions of code PACE-4 with the value of level density parameter "a" $= A/10\,\mathrm{MeV}^{-1}$, indicating these reaction channels are populated via CF process only.

The production detail of these ERs $^{137}\mathrm{Ce}$, $^{135}\mathrm{Ce}$, and $^{133}\mathrm{Ce}$ is shown by the following reaction equation:

$$^{16}\mathrm{O} + {}^{124}\mathrm{Sn} \rightarrow {}^{140}\mathrm{Ce}^* \rightarrow {}^{140\text{-}x}\mathrm{Ce} + xn(x = 3,5,7).$$

Measured cumulative and independent cross-sections for the evaporation residues $^{133}\mathrm{La}$ populated through the pxn ($x = 6$) channel have been plotted along with their PACE-4 predictions and is shown in Fig. 2(d).

The independent cross-sections have been deduced using expression given in Table II. It has been observed from this Fig. 2(d), that the measured independent cross-sections of the evaporation residue $^{133}\mathrm{La}$ are well reproduced with theoretical predictions of PACE-4 at $K = 10$. The evaporation residue $^{133}\mathrm{La}$ may be produced in CF process. This evaporation residue may be populated via two different reaction routes as follows.

Further, the sum of experimentally measured cross-sections ($\sigma^{\mathrm{meas}}_{\mathrm{SUM}(xn+pxn)}$) of evaporation residues $^{137\mathrm{m,g},135,133\mathrm{m,g}}\mathrm{Ce}$ (xn) and $^{133}\mathrm{La}$ (pxn) has been estimated and compared with the sum of theoretical cross-sections of PACE-4 ($\sigma^{\mathrm{PACE-4}}_{\mathrm{SUM}(xn+pxn)}$) for the same evaporation residues at free parameter value $K = 10$ is shown in Fig. 3. A reasonably good agreement between experimentally measured cross-sections ($\sigma^{\mathrm{meas}}_{\mathrm{SUM}(xn+pxn)}$) and PACE-4 predictions ($\sigma^{\mathrm{PACE-4}}_{\mathrm{SUM}(xn+pxn)}$) has been observed. This comparison clearly confirms the fact that the population of these evaporation residues only via CF of projectile $^{16}\mathrm{O}$ with $^{124}\mathrm{Sn}$ target. The value of level density parameter "a" $=A/10\,\mathrm{MeV}^{-1}$ can be used consistently as a fixed parameter for the analysis of all the reaction channels, which are expected to be populated via both CF and ICF reaction processes. With this optimization, the value of $K = 10$ has been taken for the further EFs data analysis of $\alpha xn/\alpha pxn/2\alpha xn/2\alpha pxn$-emiting channels in same system by taking the same set of parameters as default.

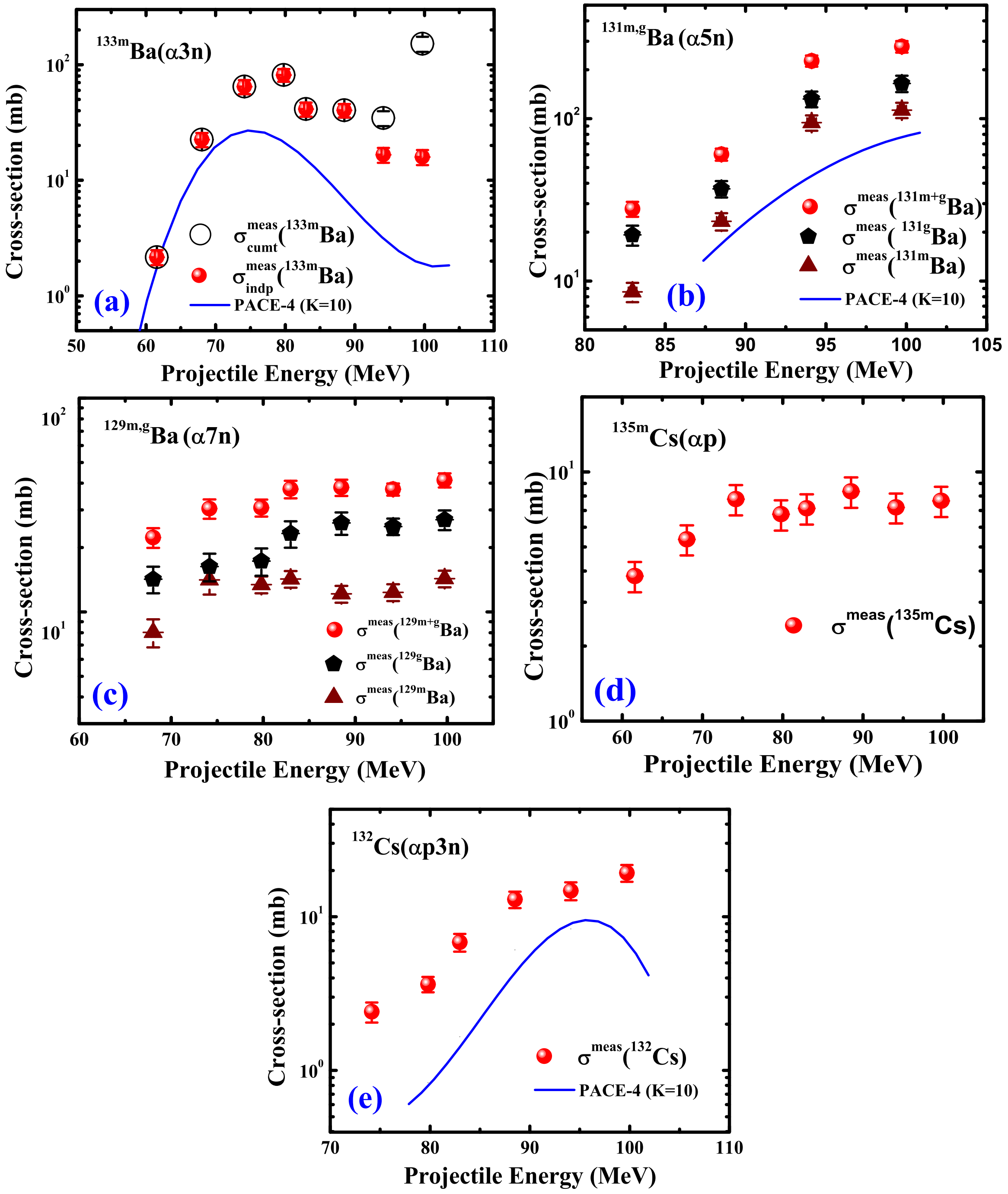

FIG. 4. Excitation functions for ERs ^{133m}Ba($\alpha 3n$), ^{131m,g}Ba($\alpha 5n$), ^{129m,g}Ba($\alpha 7n$), ^{135m}Cs(αp), and ^{132}Cs($\alpha p3n$) produced in ^{16}O + ^{124}Sn system. Solid and hollow symbols represent the measured data. The solid line corresponds to theoretical predictions of the PACE-4 code at $K = 10$.

B. αxn, αpxn, $2\alpha xn$, and $2\alpha pxn$ emission channels (ICF channels)

The excitation function of ERs produced in the reactions ^{133m}Ba($\alpha 3n$), ^{131m,g}Ba($\alpha 5n$), ^{129m,g}Ba($\alpha 7n$), ^{135m}Cs(αp), ^{132}Cs($\alpha p3n$), ^{131m}Xe($2\alpha n$), and ^{131}I($2\alpha p$) associated with α-particle(s) emission channels, which are expected to be produced mainly through the incomplete fusion process are displayed in Figs. 4 and 5 along with the measured independent cross-section values. The independent metastable state cross-sections of the evaporation residues ^{133m}Ba ($\alpha 3n$) produced in 1α-emission channel in the reactions ^{124}Sn(^{16}O,$\alpha 3n$)^{133m}Ba has also been separated out from their measured cumulative cross-sections, using the expression given in Table II. The measured EFs for the production of ER ^{133m}Ba($\alpha 3n$) corresponds to its metastable state only. The ground-state contribution could not be measured separately owing very long half-life. Hence, the total measured independent cross-sections

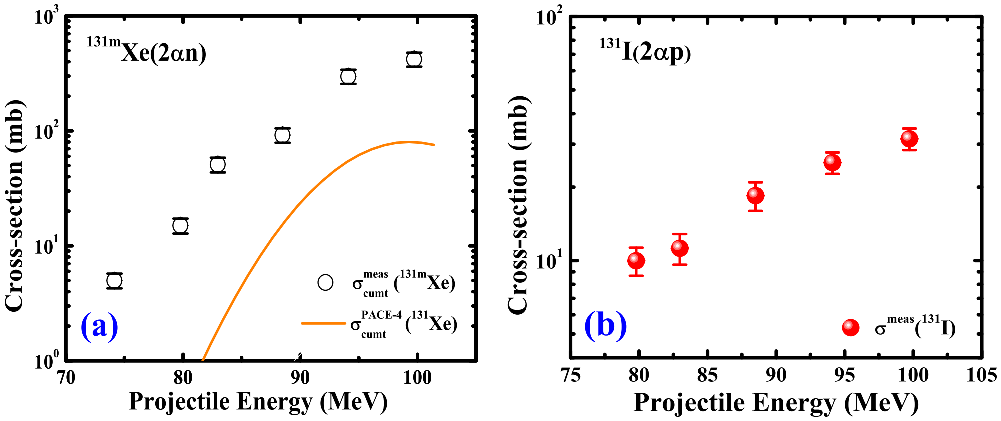

FIG. 5. Excitation functions for ERs ^{131m}Xe($2\alpha n$) and ^{131}I($2\alpha p$) produced in ^{16}O + ^{124}Sn system. Solid and hollow circles represent the measured data. The solid line corresponds to theoretical predictions of the PACE-4 code at $K = 10$.

(metastable state + ground state) may be expected to be further enhanced from the present measured independent metastable state cross-sections as compared to the PACE-4 predictions. The measured metastable independent cross-sections along with their cumulative cross-section for the production of evaporation residue ^{133}Ba compared with PACE-4 predictions, as shown in Fig. 4(a), it is observed from this figure that the measured independent EFs are much enhanced over their theoretical values. Since ICF is not considered in PACE-4 calculations, this enhancement may be attributed to the fact that this channel may be populated not only by CF of ^{16}O but also have a significant contribution from ICF of ^{16}O, i.e., fusion of fragment ^{12}C with the target ^{124}Sn (if ^{16}O breaks up into α and ^{12}C fragments). The evaporation residue ^{133m}Ba may also be formed by EC/β^+ decay of their precursor isobars ^{133}Ce ($7n$) and ^{133}La ($p6n$). The precursor decay contribution from their higher Z isobars into ER ^{133m}Ba has been determined at only projectile energy >94 MeV.

The evaporation residue ^{133m}Ba may be populated via three different reaction routes as follows:

(i) CF of ^{16}O with ^{124}Sn, i.e.,

$$^{16}\mathrm{O} + {}^{124}\mathrm{Sn} \rightarrow {}^{140}\mathrm{Ce}^* \rightarrow {}^{133}\mathrm{Ba} + \alpha + xn(x = 3),$$

(ii) ICF of ^{16}O (i.e., fusion of the fragment ^{12}C)

$$\begin{aligned} ^{16}\mathrm{O}(^{12}\mathrm{C} + {}^{4}\mathrm{He}) + {}^{124}\mathrm{Sn} &\rightarrow {}^{12}\mathrm{C} + {}^{124}\mathrm{Sn} \\ &\quad + {}^{4}\mathrm{He}/\alpha(\text{spectator}) \\ &\rightarrow {}^{136}\mathrm{Ba}^* + \alpha(\text{spectator}) \\ ^{136}\mathrm{Ba}^* &\rightarrow {}^{133}\mathrm{Ba} + xn(x = 3), \end{aligned}$$

(iii) Through EC/β^+-decay of the produced higher Z precursor isobar,

$$^{16}\mathrm{O} + {}^{124}\mathrm{Sn} \rightarrow {}^{140}\mathrm{Ce}^* \rightarrow {}^{133}\mathrm{La} + p + xn(x = 6)$$

$$^{133}\mathrm{La} \xrightarrow{EC/\beta^+} {}^{133}\mathrm{Ba}.$$

As already mentioned in Sec. III, no precursor contribution for the ERs ^{131m,g}Ba, ^{129m,g}Ba, ^{135m}Cs, and ^{132}Cs has been found. Thus, measured cross-sections of the evaporation residues ^{131m,g}Ba, ^{129m,g}Ba, ^{135m}Cs, and ^{132}Cs are independent. The measured independent cross-sections for the evaporation residues ^{131m,g}Ba and ^{132}Cs are plotted along with PACE-4 predictions in Figs. 4(b) and 4(e). The measured cross-sections of the metastable as well as ground state of ER ^{131m,g}Ba along with the sum of metastable and ground state contributions are also displayed in Fig. 4(b), The enhancement in the measured cross-sections of ERs ^{131m,g}Ba and ^{132}Cs over their theoretical predictions again indicates the presence of the ICF component along with CF as displayed in Figs. 4(b) and 4(e).

The evaporation residues ^{131m,g}Ba may be populated via two different reaction routes as follows:

(i) CF of ^{16}O with ^{124}Sn, i.e.,

$$^{16}\mathrm{O} + {}^{124}\mathrm{Sn} \rightarrow {}^{140}\mathrm{Ce}^* \rightarrow {}^{131}\mathrm{Ba} + \alpha + xn(x = 5),$$

(ii) ICF of ^{16}O (i.e., fusion of the fragment ^{12}C)

$$\begin{aligned} ^{16}\mathrm{O}(^{12}\mathrm{C} + {}^{4}\mathrm{He}) + {}^{124}\mathrm{Sn} &\rightarrow {}^{12}\mathrm{C} + {}^{124}\mathrm{Sn} \\ &\quad + {}^{4}\mathrm{He}/\alpha(\text{spectator}) \\ &\rightarrow {}^{136}\mathrm{Ba}^* + \alpha(\text{spectator}) \\ ^{136}\mathrm{Ba}^* &\rightarrow {}^{131}\mathrm{Ba} + xn(x = 5), \end{aligned}$$

and the evaporation residues ^{132}Cs may also be populated via the two different following reaction routes:

(i) CF of ^{16}O with ^{124}Sn, i.e.,

$$^{16}\mathrm{O} + {}^{124}\mathrm{Sn} \rightarrow {}^{140}\mathrm{Ce}^* \rightarrow {}^{132}\mathrm{Cs} + \alpha + pxn(x = 3),$$

(ii) ICF of ^{16}O (i.e., fusion of the fragment ^{12}C)

$$\begin{aligned} ^{16}\mathrm{O}(^{12}\mathrm{C} + {}^{4}\mathrm{He}) + {}^{124}\mathrm{Sn} &\rightarrow {}^{12}\mathrm{C} + {}^{124}\mathrm{Sn} \\ &\quad + {}^{4}\mathrm{He}/\alpha(\text{spectator}) \\ &\rightarrow {}^{136}\mathrm{Ba}^* + \alpha(\text{spectator}) \\ ^{136}\mathrm{Ba}^* &\rightarrow {}^{132}\mathrm{Cs} + pxn(x = 3). \end{aligned}$$

For the measured EFs of evaporation residues ^{129m,g}Ba and ^{135m}Cs populated via ($\alpha 7n$) and (αp) emissions channels, the theoretical prediction of code PACE-4 gives negligible cross-sections and hence are not shown in Figs. 4(c) and 4(d). Total measured cross-section (metastable state + ground state) along with metastable as well as ground state contributions for the ER

^{129m,g}Ba and only measured metastable state contribution for ^{135m}Cs are shown in Figs. 4(c) and 4(d), respectively. As can be seen from these figures, the measured independent cross-sections for these ERs are comparatively much larger than PACE-4 predictions. This large enhancement in the measured cross-sections over their theoretical predictions may again be attributed to the ICF of the projectile ^{16}O with target ^{124}Sn (if the projectile ^{16}O breaks up into fragments ^{12}C and ^{4}He). Subsequent emission of neutrons and protons during de-excitation of the composite system ^{136}Ba* leads to the production of the above evaporation residues populated via ICF process. Here, it is important to note that the measured EFs for the production of ^{135m}Cs(αp) corresponds to its metastable state only. The ground-state contribution could not be measured separately owing very long half-life. In this case, the total measured cross-sections (metastable state + ground state) would have been expected to be further enhanced after adding ground-state contribution as compared to PACE-4 predictions. The enhancement in measured cross-sections for the ERs ^{129m,g}Ba may be attributed to ICF process of the type:

$$\begin{aligned} {}^{16}\mathrm{O}({}^{12}\mathrm{C}+{}^{4}\mathrm{He})+{}^{124}\mathrm{Sn} &\rightarrow {}^{12}\mathrm{C}+{}^{124}\mathrm{Sn}+{}^{4}\mathrm{He}/\alpha(\mathrm{spectator}) \\ &\rightarrow {}^{136}\mathrm{Ba}^*+\alpha(\mathrm{spectator}) \\ {}^{136}\mathrm{Ba}^* &\rightarrow {}^{129}\mathrm{Ba}+xn(x=7). \end{aligned}$$

Similarly, the evaporation residues ^{135}Cs may be populated via ICF reaction route as follows:

$$\begin{aligned} {}^{16}\mathrm{O}({}^{12}\mathrm{C}+{}^{4}\mathrm{He})+{}^{124}\mathrm{Sn} &\rightarrow {}^{12}\mathrm{C}+{}^{124}\mathrm{Sn}+{}^{4}\mathrm{He}/\alpha(\mathrm{spectator}) \\ &\rightarrow {}^{136}\mathrm{Ba}^*+\alpha(\mathrm{spectator}) \\ {}^{136}\mathrm{Ba}^* &\rightarrow {}^{135}\mathrm{Cs}+pxn(x=0). \end{aligned}$$

The measured EFs for the evaporation residues ^{131m}Xe($2\alpha n$) and ^{131}I($2\alpha p$) are plotted and displayed in Fig. 5. The evaporation residue ^{131m}Xe may also have the contribution from their higher and lower Z precursor isobars ^{131}Ba, ^{131}Cs, and ^{131}I. These isobars may decay through $\beta^{\pm}$ and/or EC in to ER ^{131m}Xe.

The measured EFs for the production of ^{131m}Xe($2\alpha n$) corresponds to its metastable state only. The ground-state contribution could not be measured separately due to its stable state. A comparison of the measured cumulative cross-sections for the evaporation residue ^{131m}Xe along with theoretical cumulative cross-sections of PACE-4 code is shown in Fig. 5(a). The theoretical cumulative cross-sections are the sum of cross-sections calculated using code PACE-4 for ERs ^{131}Ba and ^{131}Cs. As can be seen from this figure, the measured cumulative cross-sections are much higher than the theoretical cumulative cross-section values, which indicates the presence of ICF components along with CF.

The residue ^{131m}Xe may be populated via four different reaction routes as follows:

(i) CF of ^{16}O with ^{124}Sn, i.e.,

$${}^{16}\mathrm{O}+{}^{124}\mathrm{Sn}\rightarrow{}^{140}\mathrm{Ce}^*\rightarrow{}^{131}\mathrm{Xe}+2\alpha+xn(x=1),$$

(ii) ICF of ^{16}O (i.e., fusion of the fragment ^{12}C)

$$\begin{aligned} {}^{16}\mathrm{O}({}^{12}\mathrm{C}+{}^{4}\mathrm{He})+{}^{124}\mathrm{Sn} &\rightarrow {}^{12}\mathrm{C}+{}^{124}\mathrm{Sn} \\ &\quad +{}^{4}\mathrm{He}/\alpha(\mathrm{spectator}) \\ &\rightarrow {}^{136}\mathrm{Ba}^*+\alpha(\mathrm{spectator}) \\ {}^{136}\mathrm{Ba}^* &\rightarrow {}^{131}\mathrm{Xe}+\alpha+xn(x=1), \end{aligned}$$

(iii) ICF of ^{16}O (i.e., fusion of the fragment ^{8}Be)

$$\begin{aligned} {}^{16}\mathrm{O}({}^{8}\mathrm{Be}+{}^{8}\mathrm{Be})+{}^{124}\mathrm{Sn} &\rightarrow {}^{8}\mathrm{Be}+{}^{124}\mathrm{Sn} \\ &\quad +{}^{8}\mathrm{Be}/2\alpha(\mathrm{spectator}) \\ &\rightarrow {}^{132}\mathrm{Xe}^*+2\alpha(\mathrm{spectator}) \\ {}^{132}\mathrm{Xe}^* &\rightarrow {}^{131}\mathrm{Xe}+xn(x=1), \end{aligned}$$

(iv) Through EC/$\beta^{\pm}$ -decay of the produced higher and lower Z precursor isobars,

Case I: $^{16}\mathrm{O}+{}^{124}\mathrm{Sn}\rightarrow{}^{140}\mathrm{Ce}^*\rightarrow{}^{131}\mathrm{Ba}+\alpha+5n$

$${}^{131}\mathrm{Ba}\xrightarrow{EC/\beta^+}{}^{131}\mathrm{Cs}\xrightarrow{EC/\beta^+}{}^{131}\mathrm{Xe},$$

Case II: $^{16}\mathrm{O}+{}^{124}\mathrm{Sn}\rightarrow{}^{140}\mathrm{Ce}^*\rightarrow{}^{131}\mathrm{I}+2\alpha+p$

$${}^{131}\mathrm{I}\xrightarrow{\beta^-}{}^{131}\mathrm{Xe}.$$

The theoretical prediction of PACE-4 code gives negligible cross-sections as compared to measured cross-section for the evaporation residue ^{131}I produced via $2\alpha p$ emissions channel and hence are not shown in Fig. 5(b). No precursor contribution for evaporation residues ^{131}I have been observed. Hence, measured EFs correspond to independent cross-sections. The measured cross-sections are comparatively much higher by orders of magnitude. This enhancement in the measured cross-sections over their theoretical PACE-4 predictions may again be attributed to the ICF process of the projectile ^{16}O, if ^{16}O break up into ^{8}Be and ^{8}Be fragments and fusion of ^{8}Be fragment with target ^{124}Sn and emission of one proton takes place from the composite system ^{132}Xe*. As such, the evaporation residue ^{131}I may be populated via two different ICF reaction routes of the type

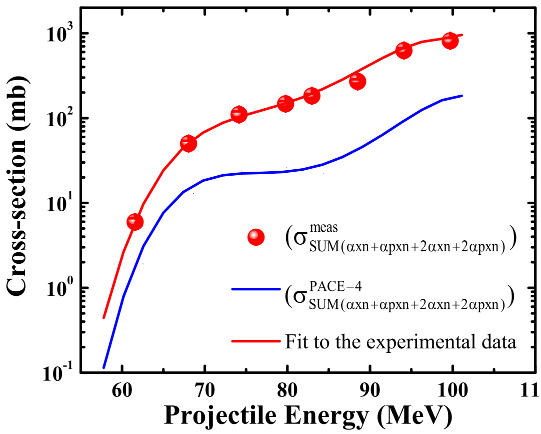

FIG. 6. Sum of all measured EFs of $\alpha xn+\alpha pxn+2\alpha xn+2\alpha pxn$ channels ($\sigma^{\mathrm{meas}}_{\mathrm{SUM}(\alpha xn+\alpha pxn+2\alpha xn+2\alpha pxn)}$) populated in ^{16}O + ^{124}Sn system along with PACE-4 predictions ($\sigma^{\mathrm{PACE-4}}_{\mathrm{SUM}(\alpha xn+\alpha pxn+2\alpha xn+2\alpha pxn)}$) at $K=10$.

(i) ICF of ^{16}O (i.e., fusion of the fragment ^{12}C)

$$\begin{aligned}
^{16}\mathrm{O}(^{12}\mathrm{C}+{}^{4}\mathrm{He})+{}^{124}\mathrm{Sn} &\rightarrow {}^{12}\mathrm{C}+{}^{124}\mathrm{Sn}\\
&\quad+{}^{4}\mathrm{He}/\alpha(\text{spectator})\\
&\rightarrow {}^{136}\mathrm{Ba}^{*}+\alpha(\text{spectator})\\
^{136}\mathrm{Ba}^{*} &\rightarrow {}^{131}\mathrm{I}+\alpha+pxn(x=0),
\end{aligned}$$

(ii) ICF of ^{16}O (i.e., fusion of the fragment ^{8}Be)

$$\begin{aligned}
^{16}\mathrm{O}(^{8}\mathrm{Be}+{}^{8}\mathrm{Be})+{}^{124}\mathrm{Sn} &\rightarrow {}^{8}\mathrm{Be}+{}^{124}\mathrm{Sn}\\
&\quad+{}^{8}\mathrm{Be}/2\alpha(\text{spectator})\\
&\rightarrow {}^{132}\mathrm{Xe}^{*}+2\alpha(\text{spectator})\\
^{132}\mathrm{Xe}^{*} &\rightarrow {}^{131}\mathrm{I}+pxn(x=0).
\end{aligned}$$

In addition to that the sum of all measured cross-sections ($\sigma^{\mathrm{meas}}_{\mathrm{SUM}(\alpha xn+\alpha pxn+2\alpha xn+2\alpha pxn)}$) of evaporation residues $^{133\mathrm{m}}$Ba, $^{131\mathrm{m,g}}$Ba, $^{129\mathrm{m,g}}$Ba, ^{135}Cs, ^{132}Cs, $^{131\mathrm{m}}$Xe, and ^{131}I populated via αxn, αpxn, $2\alpha xn$, $2\alpha pxn$ emission channels are compared with that estimated by PACE-4 code ($\sigma^{\mathrm{PACE4}}_{\mathrm{SUM}(\alpha xn+\alpha pxn+2\alpha xn+2\alpha pxn)}$) for presently studied system and is shown in Fig. 6. These plots clearly show that the measured cross-sections ($\sigma^{\mathrm{meas}}_{\mathrm{SUM}(\alpha xn+\alpha pxn+2\alpha xn+2\alpha pxn)}$) are found to be significantly enhanced over that predicted by PACE-4 ($\sigma^{\mathrm{PACE4}}_{\mathrm{SUM}(\alpha xn+\alpha pxn+2\alpha xn+2\alpha pxn)}$) in the entire projectile energy range. Moreover, it may be pointed out that the experimentally measured ERs of αxn, αpxn, $2\alpha xn$, $2\alpha pxn$ emission channels are found to be produced through the projectile break-up process (ICF reaction) in addition to CF process.

VI. SYSTEMATIC STUDIES FOR DEPENDENCE OF ICF DYNAMICS ON VARIOUS ENTRANCE CHANNEL PARAMETERS

It may not be possible to directly obtain the relative contributions of ICF from the measured EFs for the $^{16}\mathrm{O}+{}^{124}\mathrm{Sn}$ system at projectile energy $\approx$3–7 MeV/nucleon. An attempt has been made to estimate the ICF contribution from the measured excitation function data and to study the dependence of ICF dynamics on various entrance channel parameters, i.e., projectile energy, projectile structure, entrance channel mass-asymmetry, α-Q value, Coulomb factor ($Z_{\mathrm{P}}Z_{\mathrm{T}}$), and deformation parameter (β_2) of the target.

To estimate the ICF fraction for the present $^{16}\mathrm{O}+{}^{124}\mathrm{Sn}$ system, the F_{ICF} is a measure of strength of ICF relative to total fusion (CF and ICF). F_{ICF} is defined as the $F_{\mathrm{ICF}}(\%) = (\sigma^{\mathrm{ICF}}_{\mathrm{SUM}}/\sigma^{\mathrm{CF+ICF}}_{\mathrm{TF}}) \times 100$ has been deduced. The detailed description of determination of F_{ICF} is given in our earlier work [40]. The relative velocity (v_{relt}) of the nucleons in the compound system has been widely used as a normalization factor to compare the ICF fractions of different systems [17–20]. F_{ICF} of different systems are also taken at a constant value of $E_{\mathrm{lab}}/E_{\mathrm{CB}}$ for comparison [19]. This parameter reduces the effect of different Coulomb barriers. In the present work, a new factor (ℓ_{max}-ℓ_{crit})/ℓ_{max} has been introduced to understand the dependence of ICF fraction on various entrance channel parameters. The angular momentum limit of CF and ICF channels depends on this new factor. In this factor, ℓ_{max} and ℓ_{crit} are the maximum and critical angular momentum of the system, respectively, and their values calculated using prescription [27]. This factor is related to the entrance channel angular momentum of the system and, thus, is more suitable in case of the ICF dynamics where more angular momentum is involved.

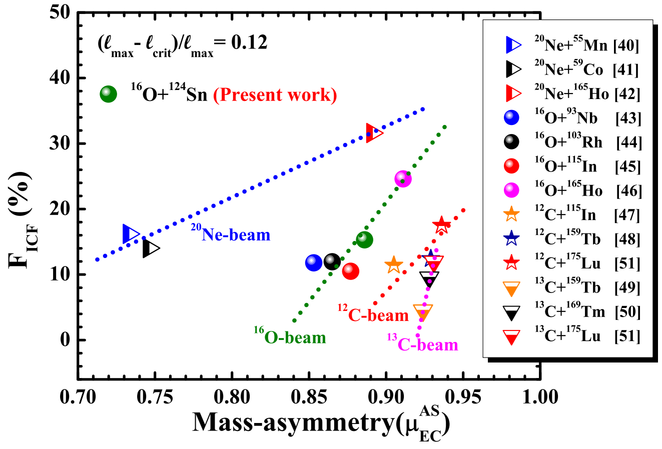

FIG. 7. The incomplete fusion fraction (F_{ICF}) for various projectile target systems as function of entrance channel mass asymmetry $\mu^{\mathrm{AS}}_{\mathrm{EC}}$ at a constant value (ℓ_{max}-ℓ_{crit})/$\ell_{\mathrm{max}} = 0.12$. The dotted lines are drawn to represent the incomplete fusion fraction (F_{ICF}) data for different projectiles.

A. Dependence of ICF dynamics on entrance channel mass asymmetry

The present EF data have also been analyzed within the framework of entrance channel mass-asymmetry systematics as suggested by Morgenstern *et al.* [15] to understand the dependence of ICF fraction on the entrance channel mass asymmetry [$\mu^{\mathrm{AS}}_{\mathrm{EC}} = A^{T}/(A^{T}+A^{P})$]. Morgenstern *et al.* [15] systematics show that the ICF dynamics contribute significantly for more mass-asymmetric system than less mass-asymmetric system. With this view, the measured incomplete fusion F_{ICF} for the present system $^{16}\mathrm{O}+{}^{124}\mathrm{Sn}$ have been compared with some earlier measurements [40–51] at a constant value (ℓ_{max}-ℓ_{crit})/$\ell_{\mathrm{max}} = 0.12$ for the different systems at a constant value of (ℓ_{max}-ℓ_{crit})/$\ell_{\mathrm{max}} = 0.12$ as a function of entrance channel mass asymmetry and are shown in Fig. 7. It is important to mention that the available data are limited for some projectiles to only a few target nuclei. This figure shows that the ICF fraction increases linearly with their mass asymmetry, separately for each projectile. The dashed lines are drawn to represent the incomplete fusion F_{ICF} fraction data for the different projectiles. The F_{ICF} is found to increase almost linearly with mass-asymmetry $\mu^{\mathrm{AS}}_{\mathrm{EC}}$, separately for each projectile. The magnitude of F_{ICF} for the nearby mass asymmetry systems $^{13}\mathrm{C}+{}^{159}\mathrm{Tb}$ ($\mu^{\mathrm{AS}}_{\mathrm{EC}} = 0.9244$), $^{12}\mathrm{C}+{}^{159}\mathrm{Tb}$ ($\mu^{\mathrm{AS}}_{\mathrm{EC}} = 0.9298$), $^{13}\mathrm{C}+{}^{169}\mathrm{Tm}$ ($\mu^{\mathrm{AS}}_{\mathrm{EC}} = 0.9286$), $^{13}\mathrm{C}+{}^{175}\mathrm{Lu}$ ($\mu^{\mathrm{AS}}_{\mathrm{EC}} = 0.9308$), and $^{12}\mathrm{C}+{}^{175}\mathrm{Lu}$ ($\mu^{\mathrm{AS}}_{\mathrm{EC}} = 0.9358$) for different projectiles are found to be $\approx$2%, 8%, 9%, 11%, and 17%, respectively. The values of F_{ICF} are found to be very different for similar mass asymmetry systems. These observations are in contrast to that ICF dependence on the degree

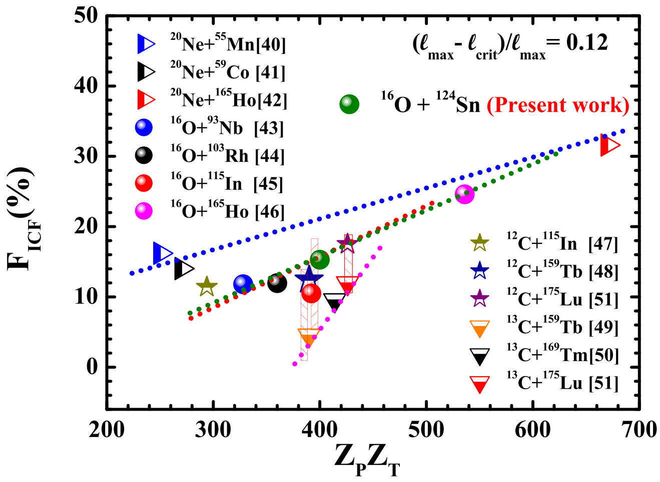

FIG. 8. Incomplete fusion fraction (F_{ICF}) of various systems as a function of Coulomb factor ($Z_P Z_T$) at constant value ($\ell_{\max}$-$\ell_{\mathrm{crit}})/\ell_{\max} = 0.12$. Dotted lines are drawn to represent the incomplete fusion fraction (F_{ICF}) data.

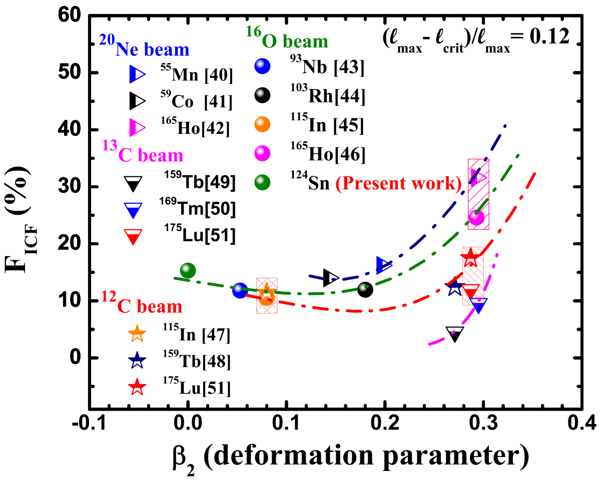

FIG. 9. Incomplete fusion fraction (F_{ICF}) of various systems as a function of deformation parameter (β_2) of target at constant value ($\ell_{\max}$-$\ell_{\mathrm{crit}})/\ell_{\max} = 0.12$. Dash dotted curves are drawn to represent F_{ICF} data for different projectiles.

of mass-asymmetry of the entrance channel as suggested by Morgenstern *et al.* [15]. In this figure, it is observed that the increasing rate of F_{ICF} fraction is different for different projectiles. As such, the present analysis indicates a projectile dependent mass-asymmetry pattern rather than a simple rise with mass asymmetry of all projectiles. These present results clearly show that the structure of projectile along with the mass asymmetry affect the ICF dynamics at these energies.

B. Dependence of ICF dynamics on Coulomb factor

As already discussed in previous subsections of this manuscript on the basis of Fig. 7, it has been noticed that the ICF fraction depends on the projectile structure and projectile dependent mass asymmetry. Therefore, these previous systematic studies inferred that ICF fraction is sensitive to the projectile energy, nature of either the projectile or the target nuclei, and entrance channel mass-asymmetry. To understand the dependence of ICF fraction on product of the projectile charge and target charge, i.e., ($Z_P Z_T$) called Coulomb factor [22–25], where Z_P and Z_T are the atomic numbers of the projectile and target nuclei, respectively. The ICF fraction has also been plotted as a function of Coulomb factor ($Z_P Z_T$) of projectile and target. The deduced ICF fraction for the present system with few earlier measurements [40–51] at a constant value ($\ell_{\max}$-$\ell_{\mathrm{crit}})/\ell_{\max} = 0.12$ have been plotted as a function of Coulomb factor ($Z_P Z_T$) and displayed in Fig. 8.

An increase in Coulomb factor ($Z_P Z_T$) will enhance the strength of Coulomb interaction during the projectile interaction with target nucleus and is related with projectile break-up probability. It can be seen from this figure that F_{ICF} is found to increase almost linearly with the Coulomb factor ($Z_P Z_T$), having different slope for different projectiles. These observations are in contrast to that ICF dependence on the Coulomb factor $Z_P Z_T$ is linear as suggested by Shuaib *et al.* [17]. In the present analysis of F_{ICF} with $Z_P Z_T$, it can be seen that the systems with ^{20}Ne projectile show a smaller slope and the systems with ^{16}O and ^{12}C projectiles show similar slope, whereas ^{13}C projectile is having a greater slope. Here, it is interesting that ^{20}Ne has less negative α-Q value (-4.73 MeV), ^{16}O and ^{12}C have almost same α-Q value (-7.15 and -7.36 MeV), and ^{13}C has more negative α-Q value (-10.64 MeV). As such, the present analysis indicates a projectile-dependent pattern rather than a simple linear rise with Coulomb factor $Z_P Z_T$. From this figure, it has also been noticed that the projectile target systems, which have same or almost same charge product $Z_P Z_T$, the values of F_{ICF} fraction are significantly different for different projectiles at the present studied energy range. Some systems, which have same or almost same $Z_P Z_T$ values are marked by vertical rectangular boxes and shown in Fig. 8. These observations indicate that ICF dynamics may depend on different entrance channel parameters.

C. Dependence of ICF dynamics on deformation parameter (β_2)

To understand the role of target deformation on ICF dynamics, the deduced ICF fraction for the present system along with some other systems mentioned in Sec. VI B of this manuscript, at a constant ($\ell_{\max}$-$\ell_{\mathrm{crit}})/\ell_{\max} = 0.12$ have been plotted for different projectiles as a function of deformation parameter (β_2) of the target nucleus as shown in Fig. 9. Here, it is important to mention that the shape of an axially symmetric deformed nucleus is described by the deformation parameter (β_2) and directly connected to the quadruple moment (Q_0). Detailed description and formulation about deformation parameter (β_2) is given in Ref. [52]. The values of deformation parameter (β_2) for different target nuclei are taken from Ref. [53]. As can be seen from the Fig. 9 that the value of F_{ICF} follows a systematics exponential growth with increasing the deformation parameter (β_2), but the rising rate of F_{ICF} fraction are different for different projectiles, in general. These observations indicate that the ICF fraction also depends on projectile structure along with deformation of the target nuclei. However, the value of F_{ICF} for ^{16}O + ^{103}Rh system is slightly away from the

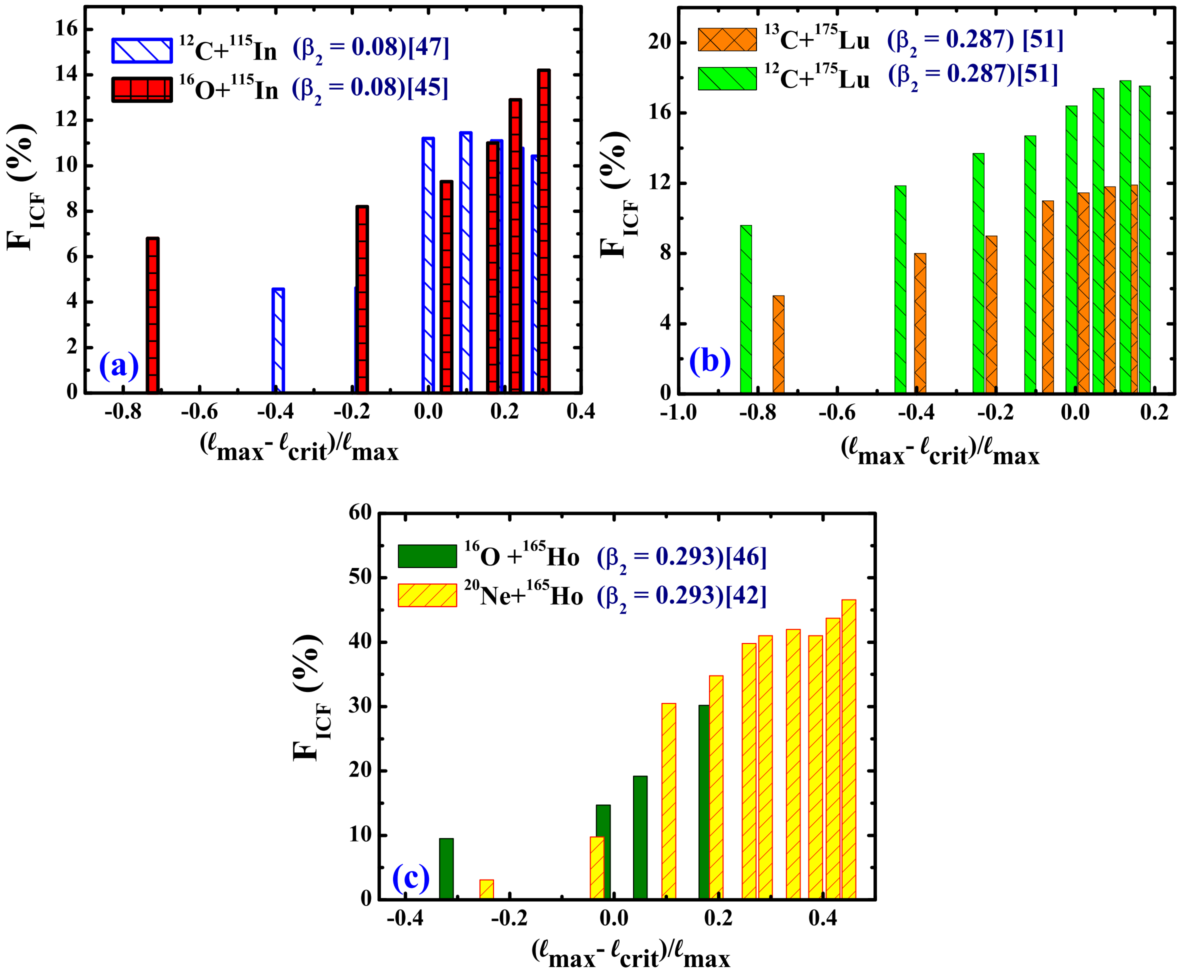

FIG. 10. Comparison of incomplete fusion fraction (F_{ICF}) as a function of (ℓ_{max}-ℓ_{crit})/ℓ_{max} for different projectile target systems, with the same deformation parameter (β_2).

increasing trend shown with the curved dash-dotted line. It may be because of the fact that in case of ^{16}O + ^{103}Rh system all α-emitting channels could not be measured due to their short half-lives and/or very low γ intensities. The present value of F_{ICF} for ^{16}O + ^{103}Rh system is expected to go up if all possible α-emitting channels could be measured. Further, some systems, which have same and almost same deformation parameter (β_2) values, marked by vertical rectangular boxes are shown in Fig. 9.

The percentages of ICF fraction for these projectile target systems are also significantly different. As a representative case, the ICF fraction along with different projectile-target systems having the same or almost the same deformation parameter (β_2) of the target nucleus has been plotted in Figs. 10(a)–10(c). In Fig. 10(a), ICF fraction for ^{16}O + ^{115}In ($\beta_2 = 0.08$) and ^{12}C + ^{115}In ($\beta_2 = 0.08$) systems are found different for similar values of deformation parameter (β_2) of target nucleus. The values of F_{ICF} fraction for the ^{12}C + ^{115}In system are larger than that of ^{16}O + ^{115}In system (except for a few energies cross sections are larger for ^{16}O). The observed large ICF fractions for ^{12}C + ^{115}In ($\mu_{\mathrm{EC}}^{\mathrm{AS}} = 0.905$) system may be explained on the basis of its larger mass asymmetry than the ^{16}O + ^{115}In ($\mu_{\mathrm{EC}}^{\mathrm{AS}} = 0.876$) system.

In Fig. 10(b), the values of F_{ICF} fraction for the ^{12}C + ^{175}Lu ($\beta_2 = 0.286$) system are significantly larger than that of ^{13}C + ^{175}Lu ($\beta_2 = 0.286$) system. The β_2 values (of target) for these systems are the same. In this case, the magnitude of the ICF fraction is decided by the α-Q value of the projectile. It may be noticed from Fig. 10(c) that the F_{ICF} fraction for the ^{20}Ne + ^{165}Ho ($\beta_2 = 0.293$) are much larger as compared to ^{16}O + ^{165}Ho ($\beta_2 = 0.293$) system, while for these systems, the deformation parameter (β_2) values are equal. The α-Q value for the projectile ^{20}Ne is less negative than projectile ^{16}O and projectile dependent mass asymmetry for the system ^{20}Ne + ^{165}Ho is larger than that of ^{16}O + ^{165}Ho. Therefore, it is expected to have a larger magnitude of ICF fraction for ^{20}Ne + ^{165}Ho system than that of ^{16}O + ^{165}Ho system. Further, these present observations may be explained on the basis of α-Q value for the projectile ^{20}Ne and projectile dependent mass-asymmetry. The present results indicate that the ICF dynamics cannot be explained on the basis of only a single parameter, i.e., deformation parameter (β_2). The present systematic of deformation parameters also show that the ICF dynamics not only affected by the deformation of target, but it also affected by other entrance channel parameters like projectile energy, projectile structure, entrance channel mass-asymmetry, α-Q

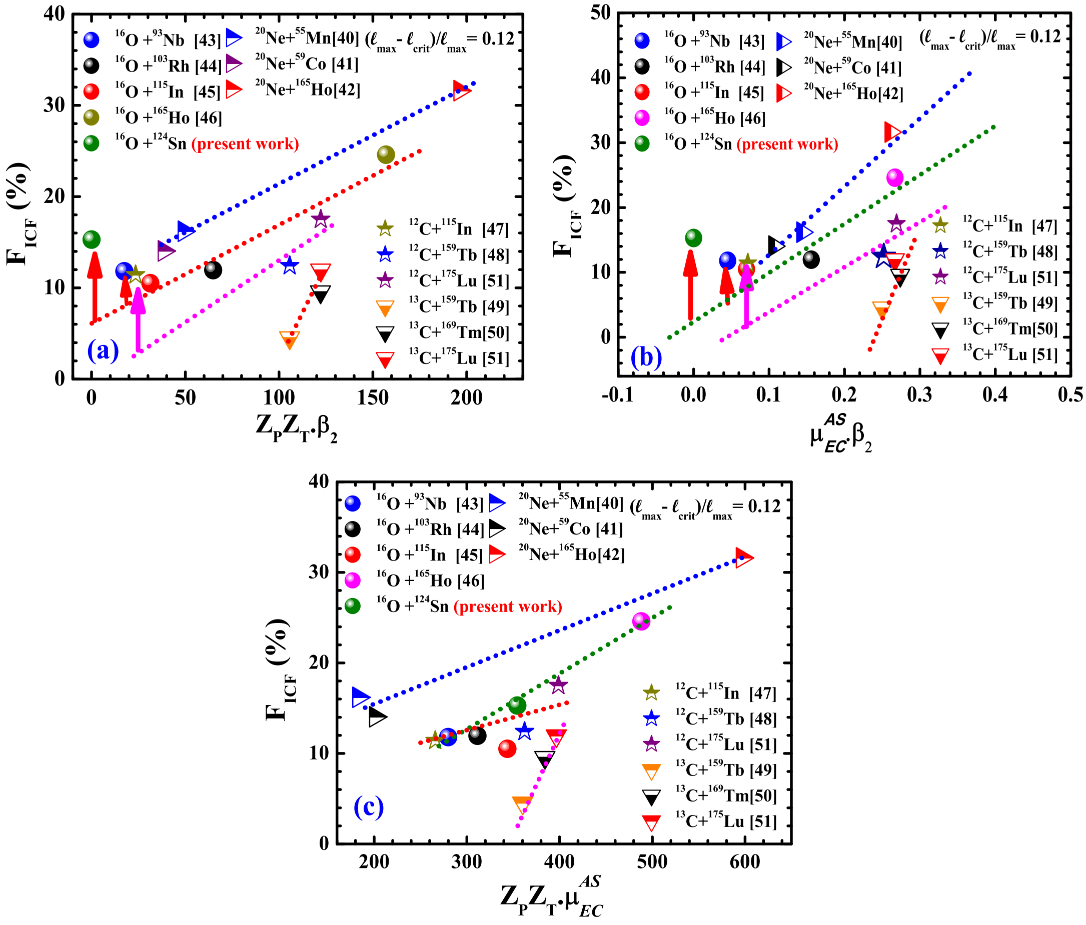

FIG. 11. Incomplete fusion fraction (F_{ICF}) as a function of (a) $Z_P Z_T \cdot \beta_2$ (b)$\mu_{EC}^{AS} \cdot \beta_2$ and (c) $Z_P Z_T \cdot \mu_{EC}^{AS}$ for different projectile target systems at a constant value of $(\ell_{\max}\text{-}\ell_{\mathrm{crit}})/\ell_{\max} = 0.12$.

value of the projectile, and Coulomb factor ($Z_P Z_T$) in the entire energy range. These experimental observations are very important and may be useful for the prediction of incomplete fusion dynamics. Further, to establish dependency of F_{ICF} on deformation parameter more experimental data using HI projectiles with same Z (deformed and spherical) target nuclei are required.

D. Dependence of ICF dynamics on combinations of entrance channel parameters

As discussed earlier in Secs. VI A–VI C of this paper, from the study of the dependence of ICF dynamics on entrance channel mass asymmetry ($\mu_{\mathrm{EC}}^{\mathrm{AS}}$), Coulomb factor ($Z_P Z_T$), and deformation parameter (β_2), it has been found that the ICF dynamics does not depend completely on a single entrance channel parameter or it cannot be explain through only a single entrance channel parameter. Further, an attempt has been made to investigate the dependence of ICF dynamics on these parameters by taking various combinations of entrance channel parameters, namely; $Z_P Z_T \cdot \beta_2$, $\mu_{\mathrm{EC}}^{\mathrm{AS}} \cdot \beta_2$, and $Z_P Z_T \cdot \mu_{\mathrm{EC}}^{\mathrm{AS}}$. Kumar *et al.* [18] has suggested a combination of parameter $Z_P Z_T \cdot \beta_2$ and observed the dependence of ICF on this parameter. According to this systematic study, ICF fraction shows a linear growth with the $Z_P Z_T \cdot \beta_2$ for different projectile target combinations at a constant value of (v_{relt}). With this in view, the incomplete fusion fraction (F_{ICF}) has been plotted as function of $Z_P Z_T \cdot \beta_2$ for the present system along with other systems as discussed above in Secs. VI A–VI C and is shown in Fig. 11(a). It may be noticed from this figure that F_{ICF} increases linearly with $Z_P Z_T \cdot \beta_2$ for different projectiles, independently. These results are similar as suggested by Ref. [18] for the systems having highly deformed targets. But the F_{ICF} is deviating from the linear growth in case of spherical or slightly deformed targets. This is due to the fact that in the case of spherical targets, the value of deformation parameter (β_2) is zero. If this value of β_2 ($= 0$) multiplied with any other parameter, it makes the whole term zero. As such, no systematic pattern will be observed for the spherical and slightly deformed target. Further, to confirm the above observations, another parameter $\mu_{\mathrm{EC}}^{\mathrm{AS}} \cdot \beta_2$ has been taken. In this respect, a graph of F_{ICF} as function of $\mu_{\mathrm{EC}}^{\mathrm{AS}} \cdot \beta_2$ for the present system along with other systems has been plotted and is displayed in Fig. 11(b). The results are found to be similar as observed for F_{ICF} versus $Z_P Z_T \cdot \beta_2$. On the basis of these results, the deformation parameter (β_2) of the target should be considered as an independent parameter, which affects the ICF dynamics. But it should not be multiplied with any other entrance channel parameters to explain the complete characteristics of ICF dynamics.

To understand the complete gross features of the ICF dependence on various entrance channel parameters, a new entrance channel parameter $Z_PZ_T \cdot \mu_{EC}^{AS}$ has been taken as a combination of Z_PZ_T and μ_{EC}^{AS}. A graph of F_{ICF} as a function of $Z_PZ_T \cdot \mu_{EC}^{AS}$ has been plotted and is shown in Fig. 11(c) to investigate the dependences of ICF on this new combined parameter. As can be seen clearly from this figure that the ICF fraction increases linearly with $Z_PZ_T \cdot \mu_{EC}^{AS}$, but it has different slopes for different projectiles. This pattern is also similar as observed for F_{ICF} versus Z_PZ_T and μ_{EC}^{AS} individually for different projectiles. The multiplication of these two parameters should also retain same characteristics. It means that the combined parameter $Z_PZ_T \cdot \mu_{EC}^{AS}$ is able to explain the ICF dynamics in place of two parameters Z_PZ_T and μ_{EC}^{AS}. As a comparison of F_{ICF} plots, this parameter explains ICF dynamics with more consistency than that of Z_PZ_T. Here it is also important to mention that the different slopes of F_{ICF} for different projectiles have been observed. It may be due to the projectile α-Q value effect on ICF. The present results indicate that the combination of parameters $Z_PZ_T \cdot \beta_2$ and $\mu_{EC}^{AS} \cdot \beta_2$ are not suitable to explain the whole characteristics of ICF dynamics, especially for spherical and slightly deformed targets. The new combined parameter $Z_PZ_T \cdot \mu_{EC}^{AS}$ completely explains the ICF dynamics more precisely than that of other entrance channel parameters.

VII. SUMMARY AND CONCLUSIONS

Excitation functions of eleven evaporation residues populated through complete and/or incomplete fusion reaction have been measured in the $^{16}O + ^{124}Sn$ system in the projectile energy range $\approx 3-7$ MeV/nucleon. It has been found that some of the evaporation residues populated through complete and/or incomplete fusion have contribution from their precursor decay of higher or lower charge isobars during the decay curve analysis. The independent production cross-section and precursor decay contribution have been separated out from their measured cumulative cross-sections. The experimentally measured EFs have been compared with predictions of statistical model code PACE-4 based on compound nucleus theory. The experimentally measured EFs of evaporation residues populated through xn/pxn-emitting channels are found to be satisfactorily reproduced with the statistical model predictions PACE-4, indicating their production through CF only. A significant enhancement in the measured excitation functions over their theoretical predictions of PACE-4 for the all evaporation residues populated through α-particle(s) emitting channel has been found. This enhancement may be attributed to the occurrence of incomplete fusion involving break-up of projectile ^{16}O into $^{12}C + ^{4}He$ and /or $^{8}Be + ^{8}Be$ followed by fusion of one of the fragments with the target nucleus ^{124}Sn. Hence, it is inferred that incomplete fusion plays an important role in the production of ERs involving single or cluster of α-particle emission at these beam energies. The present findings of ERs populated via CF and/or ICF are also consistent with our earlier measurements using particle-γ-coincidence technique for same system at projectile energy ≈ 6.2 MeV/nucleon [54]. Moreover, dependence of ICF dynamics on various entrance channel parameters namely; entrance channel mass-asymmetry (μ_{EC}^{AS}), Coulomb factor (Z_PZ_T), and deformation parameter (β_2) of the target have been studied. Further, to have a better insight into the role of these entrance channel parameters, the values of incomplete fusion fraction for some other systems taken from literature are compared. In general, the magnitudes of F_{ICF} values are found to increase with the μ_{EC}^{AS}, Z_PZ_T, and β_2, independently for different projectiles. It may be inferred that from these results that the contribution of ICF is not only affected by μ_{EC}^{AS}, Z_PZ_T, and β_2, but it is also affected by the structure of projectile. It has also been observed that the projectile target systems, which have the same or almost the same Coulomb factor (Z_PZ_T), and the values of F_{ICF} fraction are significantly different in the energy range of the present study. These results indicate that F_{ICF} fraction does not follow any systematic pattern with increasing the Coulomb factor (Z_PZ_T). It means that the Coulomb factor does not fully affect the ICF dynamics at low projectile energy. In addition, the F_{ICF} follows a systematic exponential growth with increasing the deformation parameter (β_2) of target, but the rising rates of F_{ICF} are different for different projectiles. The present results clearly indicate that the deformation of target along with the other entrance channel parameters affect the ICF dynamics at respective energies. Again, the present results indicate that the ICF is also found to be sensitive to projectile structure and α-Q value of the projectile. For better understanding, an attempt has been made to investigate the dependence of ICF dynamics on above discussed entrance channel parameters by taking various combinations of them, namely, $Z_PZ_T \cdot \beta_2$, $\mu_{EC}^{AS} \cdot \beta_2$, and $Z_PZ_T \cdot \mu_{EC}^{AS}$. It has been found that F_{ICF} increases linearly with these three combined parameters $Z_PZ_T \cdot \beta_2$, $\mu_{EC}^{AS} \cdot \beta_2$, and $Z_PZ_T \cdot \mu_{EC}^{AS}$, independently for different projectiles. But the F_{ICF} deviates from the linear pattern for spherical or slightly deformed targets with $Z_PZ_T \cdot \beta_2$ and $\mu_{EC}^{AS} \cdot \beta_2$. In conclusions, the deformation parameter (β_2) of the target should be considered as an individual parameter, which affects the ICF dynamics. But it should not be multiplied with any other entrance channel parameters to explain the whole characteristics of ICF dynamics. These results are in contrast with Ref. [18]. No such inconsistency has been observed with $Z_PZ_T \cdot \mu_{EC}^{AS}$. These present results further indicate that the parameters $Z_PZ_T \cdot \beta_2$ and $\mu_{EC}^{AS} \cdot \beta_2$ are not suitable to justify the complete characteristic of ICF dynamics, particularly for spherical and slightly deformed targets. The combined parameter $Z_PZ_T \cdot \mu_{EC}^{AS}$ has been found to explain the ICF dynamics more precisely as compared to other entrance channel parameters.

On the basis of the present results, it may be concluded that the ICF dynamics strongly depends on various entrance channel parameters and their combinations. The present systematic study suggests that the features of ICF dynamics can be explained in better way through the combination of Z_PZ_T and μ_{EC}^{AS}. These results observed in the present study are very new and interesting. More research work is required to probe a single entrance channel parameter, which will be able to explain the gross features of ICF dynamics at low projectile energy.

ACKNOWLEDGMENTS

The authors are thankful to Dr. D. Kanjilal, Director and Dr. Sundeep Chopra, Convener, AUC, Inter University Accelerator Centre (IUAC), New Delhi, India, for providing the necessary experimental facilities to carry out the experiments. The authors are also thankful to Target Lab In charge, Mr. S. R. Abhilash, and operational staff of Pelletron Accelerator, IUAC, New Delhi, for providing good co-operation during the course of this experiment. D.S. acknowledges encouragement from the Vice-Chancellor of Central University of Jharkhand (CUJ), Ranchi, India. Authors express their thanks to the Head, Centre for Applied Physics, CUJ, Ranchi, for providing the necessary facilities during the present work. D.S. is also thankful to the University Grant Commission (UGC), New Delhi, India, for providing financial support through UGC-BSR startup Grant No. F.30-14/2014(BSR) and IUAC, New Delhi research project (Ref. No. IUAC/XIII.3A/UFR/54321), respectively. S.B.L. acknowledges the UGC for providing financial support through RGNFST (Reg. No. RGNF-2014-15-ST-JHA-60266).

[1] D. J. Parker, J. J. Hogan, and J. Asher, Phys. Rev. C **35**, 161 (1987).

[2] B. S. Tomar, A. Goswami, A. V. R. Reddy, S. K. Das, P. P. Burte, S. B. Manohar, and S. Prakash, Z. Phys. A **343**, 223 (1992).

[3] P. Vergani, E. Gadioli, E. Vaciago, E. Fabrici, E. Gadioli Erba, M. Galmarini, G. Ciavola, and C. Marchetta, Phys. Rev. C **48**, 1815 (1993).

[4] M. Crippa, E. Gadioli, P. Vergani, G. Ciavola, C. Marchetta, and M. Bonardi, Z. Phys. A **350**, 121 (1994).

[5] B. B. Kumar, A. Sharma, S. Mukherjee, S. Chakrabarty, P. K. Pujari, B. S. Tomar, A. Goswami, S. B. Manohar, and S. K.Datta, Phys. Rev. C **59**, 2923 (1999).

[6] M. Dasgupta, P. R. S. Gomes, D. J. Hinde, S. B. Moraes, R. M. Anjos, A. C. Berriman, R. D. Butt, N. Carlin, J. Lubian, C. R. Morton, J. O. Newton, and A. Szanto de Toledo, Phys. Rev. C **70**, 024606 (2004).

[7] P. R. S. Gomes, I. Padron, M. D. Rodriguez, G. V. Marti, R. M. Anjos, J. Lubian, R. Veiga, R. L. Neto, E. Crema, N. Added, L. C. Chamon, J. O. Fernandez Niello, O. A. Capurro, A. J. Pacheco, J. E. Testoni, D. Arbiola, A. Arazi, M. Ramirez, and M. S. Hussein, Phys. Lett. B **601**, 20 (2004).

[8] D. Singh, R. Ali, M. A. Ansari, M. H. Rashid, R. Guin, and S. K. Das, Phys. Rev. C **79**, 054601 (2009).

[9] D. Singh, M. Afzal Ansari, R. Ali, N. P. M. Sathik, and M. Ismail, J. Phys. Soc. Jpn. **75**, 104201 (2006).

[10] J. H. Barker, J. R. Beene, M. L. Halbert, D. C. Hensley, M. Jaaskelainen, D. G. Sarantites, and R. Woodward, Phys. Rev. Lett. **45**, 424 (1980).

[11] D. J. Parker, J. J. Hogan, and J. Asher, Phys. Rev. C **39**, 2256 (1989).

[12] T. Inamura, T. Kojima, T. Nomura, T. Sugitate, and H. Utsunomiya, Phys. Lett. B **84**, 71 (1979).

[13] W. Trautmann, Ole Hansen, H. Tricoire, W. Hering, R. Ritzka, and W. Trombik, Phys. Rev. Lett. **53**, 1630 (1984).

[14] D. Hojman, M. A. Cardona, A. Arazi, O. A. Capurro, J. O. Fernandez-Niello, G. V. Mart´, A. J. Pacheco, J. E. Testoni, D. Bazzacco, A. Burlon, J. Davidson, M. Davidson, G. de Angelis, M. De Poli, M. E. Debray, A. Gadea, A. J. Kreine, S. M. Lenzi, S. Lunardi, N. H. Medina, D. R. Napoli, C. Rossi Alvarez, and C. Ur, G. Phys. Rev. C **73**, 044604 (2006).

[15] H. Morgenstern, W. Bohen, W. Galster, K. Grabisch, and A. Kyanowski, Phys. Rev. Lett. **52**, 1104 (1984).

[16] S. Chakrabarty, B. S. Tomar, A. Goswami, G. K. Gubbi, S. B. Manohar, A. Sharma, B. B. Kumar, and S. Mukherjee, Nucl. Phys. A **678**, 355 (2000).

[17] M. Shuaib, V. R. Sharma, A. Yadav, P. P. Singh, M. K. Sharma, D. P. Singh, R. Kumar, R. P. Singh, S. Muralithar, B. P. Singh, and R. Prasad, Phys. Rev. C **94**, 014613 (2016).

[18] H. Kumar, S. A. Tali1, M. Afzal Ansari, D. Singh, R. Ali, K. Kumar, N. P. M. Sathik, A. Ali, S. Parashari, R. Dubey, I. Bala, R. Kumar, R. P. Singh, and S. Muralithar, Eur. Phys. J. A **54**, 47 (2018).

[19] A. Yadav, P. P. Singh, M. Shuaib, V. R. Sharma, I. Bala, Unnati, S. Gupta, D. P. Singh, M. K. Sharma, R. Kumar, S. Muralithar, R. P. Singh, B. P. Singh, and R. Prasad, Phys. Rev. C **96**, 044614 (2017).

[20] S. A. Tali, H. Kumar, M. A. Ansari, A. Ali, D. Singh, R. Ali, P. K. Giri, S. B. Linda, S. Parashari, R. Kumar, R. P. Singh, and S. Muralithar, Nucl. Phys. A **970**, 208 (2018).

[21] T. Udagawa and T. Tamura, Phys. Rev. Lett. **45**, 1311 (1980).

[22] J. Wilczynski, K. Siwek-Wilczynska, J. Van Driel, S. Gonggrijp, D. C. J. M. Hageman, R. V. F. Janssens, J. Lukasiak, R. H. Siemssen, and S. Y. Van der Werf, Nucl. Phys. A **373**, 109 (1982).

[23] M. C. Mermaz, R. Dayras, J. Barrette, B. Berthier, D. M. D. Castro Rizzo, O. Cisse, R. Legrain, A. Pagano, E. Pollacco, H. Delagrange W. Mittig, B. Heusch, G. Lanzano, and A. Palmeri, Nucl. Phys. A **441**, 129 (1985).

[24] J. P. Bondrof, J. N. De, G. Fai, A. O. T. Karvinen, B. Jakobsson, and J. Randrup, Nucl. Phys. A **333**, 285 (1980).

[25] R. Weiner and M. Westrom, Nucl. Phys. A **286**, 282 (1977).

[26] D. H. E. Gross and J. Wilczynski, Phys. Lett. B **67**, 1 (1977).

[27] A. Gavron, Phys. Rev. C **21**, 230 (1980).

[28] The Stopping and Range of Ions in Matter (SRIM-2008.04), https://www.srim.org.

[29] B. P. Ajith Kumar, E. T. Subramaniam, K. Singh, and R. K.Bhowmik, DAE-BRNS Nucl. Phys. Symp., Kolkata (2001), http://www.iuac.res.in/NIAS/.

[30] S. Y. F. Chu, L. P. Ekstrom, and R. B. Firestone, The Lund/LBNL Nuclear Data Search (LBNL, Berkeley, CA, Version 2.0, 1999), http://nucleardata.nuclear.lu.se/toi/index.asp.

[31] National Nuclear Data Centre, Brookhaven National Laboratory. https://www.nndc.bnl.gov/chart/chartNuc.jsp.

[32] M. A. Ansari, R. K. Y. Singh, M. L. Sehgel, V. K. Mittal, D. K. Avasthi, and I. M. Govil, Ann. Nucl. Energy **11**, 607 (1984).

[33] M. Cavinato, E. Fabrici, E. Gadioli, E. Gadioli Erba, P. Vergani, M. Crippa, G. Colombo, I. Redaelli, and M. Ripamonti, Phys. Rev. C **52**, 2577 (1995).

[34] R. Bass, Nucl. Phys. A **231**, 45 (1974).

[35] F. D. Becchetti, Jr. and G. W. Greenlees, Phys. Rev. **182**, 1190 (1969).

[36] P. M. Endt, Atomic Data. Nucl. Data Tables **26**, 47 (1981).

[37] A. H. Wapstra and G. Audi, Nucl. Phys. A **432**, 55 (1985).

[38] R. D. Evans, *The Atomic Nucleus* (McGraw-Hill, New York, 1982).

[39] J. P. Lestone, Phys. Rev. C **53**, 2014 (1996).

[40] Rahbar Ali, D. Singh, M. Afzal Ansari, M. H. Rashid, R. Guin, and S. K. Das, J. Phys. G: Nucl. Part. Phys. **37**, 115101 (2010).

[41] D. Singh, R. Ali, M. Afzal Ansari, B. S. Tomar, M. H. Rashid, R. Guin, and S. K. Das, Phys. Rev. C **83**, 054604 (2011).

[42] D. Singh, Rahbar Ali, M. Afzal Ansari, M. H. Rashid, R. Guin, and S. K. Das, Nucl. Phys. A **879**, 107 (2012).

[43] A. Sharma, B. B. Kumar, S. Mukherjee, S. Chakrabarty, B. S. Tomar, A. Goswami, and S. B. Manohar, J. Phys. G: Nucl. Part. Phys. **25**, 2289 (1999).

[44] U. Gupta, P. P. Singh, D. P. Singh, M. K. Sharma, A. Yadav, R. Kumar, B. P. Singh, and R. Prasad, Nucl. Phys. A **811**, 77 (2008).

[45] K. Kumar, T. Ahmad, S. Ali, I. A. Rizvi, A. Agarwal, R. Kumar, and A. K. Chaubey, Phys. Rev. C **88**, 064613 (2013).

[46] K. Kumar, T. Ahmad, S. Ali, I. A. Rizvi, A. Agarwal, R. Kumar, K. S. Golda, and A. K. Chaubey, Phys. Rev. C **87**, 044608 (2013).

[47] S. Mukherjee, A. Sharma, S. Sodaye, A. Goswami and B. S. Tomar, Int. J. Mod. Phys. E **15**, 237 (2006).

[48] A. Yadav, V. R. Sharma, P. P. Singh, D. P. Singh, M. K. Sharma, U. Gupta, R. Kumar, B. P. Singh, R. Prasad, and R. K. Bhowmik, Phys. Rev. C **85**, 034614 (2012).

[49] A. Yadav, V. R. Sharma, P. P. Singh, R. Kumar, D. P. Singh, Unnati, M. K. Sharma, B. P. Singh, and R. Prasad, Phys. Rev. C **86**, 014603 (2012).

[50] V. R. Sharma, A. Yadav, P. P. Singh, D. P. Singh, S. Gupta, M. K. Sharma, I. Bala, R. Kumar, S. Murlithar, B. P. Singh, and R. Prasad, Phys. Rev. C **89**, 024608 (2014).

[51] H. Kumar, S. A. Tali, M. A. Ansari, D. Singh, R. Ali, K. Kumar, N. P. M. Sathik, S. Parashari, A. Ali, R. Dubey, I. Bala, R. Kumar, R. P. Singh, and S. Muralithar, Nucl. Phys. A **960**, 53 (2017).

[52] S. Raman, C. W. Nestor, and P. Tikkanen, Atom. Data Nucl. Data Tables **78**, 1 (2001).

[53] P. Moller, J. R. Nix, W. D. Myers, and W. J. Swiatecki, Atom. Data Nucl. Data Tables **59**, 185 (1995).

[54] D. Singh, R. Ali, M. A. Ansari, K. S. Babu, P. P. Singh, M. K. Sharma, B. P. Singh, R. K. Sinha, R. Kumar, S. Muralithar, R. P. Singh, and R. K. Bhowmik, Phys. Rev. C **81**, 027602 (2010).